The effect of star formation algorithms on the morphology of isolated galactic disc models

by

Maan H Hani

A THESIS SUBMITTED IN PARTIAL FULFILMENT OF
THE REQUIREMENTS FOR THE DEGREE OF

BACHELOR OF SCIENCE

in

Honours Astrophysics

(Department of Astronomy and Physics, Dr. Robert Thacker supervising faculty)

.....
.....
.....
.....
.....

SAINT MARY'S UNIVERSITY

March 18^{th}, 2013

© Maan H Hani, 2013

Abstract

The effect of star formation algorithms on the morphology of isolated galactic disc models

by *Maan H Hani*

submitted on March 18^{th}, 2013:

Structure is found in the Universe on various scales ranging from galaxies to galaxy clusters, super clusters... This structure is believed to have formed in a bottom-up hierarchical way. Computational techniques allow us to model structure formation and improve our understanding of structure formation. Moreover, cosmological simulations and simulations of galaxy formation and evolution have resolutions orders of magnitude higher than the scales at which stars form. Therefore, the application of a convergent flow criterion in galaxy formation simulations is debatable. Two isolated galactic discs (280,000 particles each) and two collapsing clouds (with a NFW dark matter density profile, 100,000 particles each) were simulated for 1.02Gyr and 4.4Gyr respectively. Each pair of simulations differed in the star formation conditions. One model allowed star formation in collapsing regions only (negative velocity divergence), while the other had no such condition. Although both models had similar star formation rates, the two models also showed significant morphological differences. With the removal of the velocity divergence criterion more stars were formed and a wider spread in the stellar spatial distribution in the potential well was detected.

The removal of the divergence criterion also limited the highest allowed gas densities, and populated the halo with hot diffuse gas due to shock heating and the feedback processes. More work, particularly simulations that begin from cosmological initial conditions, is required to better understand the impact of the divergence criterion.

Contents

Chapter 1

INTRODUCTION

The understanding of the formation and evolution of the Universe is one of the most interesting topics of astrophysics. Cosmological structure is observed in the Universe on various scales ranging from galaxy components to super clusters. Cosmologists try to model and understand the initial conditions and processes controlling the transformation of linear perturbations into non-linear complex structures that we observe today in the Universe. With modern advanced observational equipment and computational techniques, cosmologists are a step closer to understanding the formation and evolution of the Universe.

This variety of densities and structures observed in today's Universe evolved from slight inhomogeneities observed in the cosmic microwave background radiation (CMBR). The CMBR consists of photons scattered at what is referred to as the surface of last scattering. The surface of last scattering is considered to be a sphere centered at earth where the cosmic microwave background (CMB) photons were last scattered. The CMBR dates back to the epoch of recombination, when electrons combined with nuclei of hydrogen and helium which caused the opacity of the Universe to drop allowing the photons to travel unhindered (e.g. Carroll and Ostlie 2007).

To better understand how the homogeneous Universe observed in the CMBR evolved to what we observe today, we need to trace cosmological evolution and the

structure of the current Universe. Observations show galaxies consisting of gas, in the form of the interstellar medium (ISM), as well as stars. Although some of a galaxy's mass is visible (luminous), observations show that galaxies appear to have mass distributions different than those of the visible mass (Freeman 1970, Rubin and Ford 1970). Rotation curves of spiral galaxies suggest that a remarkable portion of the mass is unaccounted for. Also, studies of the orbital motion of galaxies in clusters can give a good estimate of the cluster's gravitational mass. Comparing the cluster's gravitational mass to its luminous mass (galactic and X-ray gas), one can show that there is still mass that is unaccounted for. This invisible mass is known as dark matter. Dark matter is thought to be non-self interacting and hence collisionless. It is gravitationally dominant on scales larger than galactic cores (Blumenthal et al 1984). Historically, two distinct models for dark matter have been proposed. The most successful model is the cold dark matter (CDM) model which considers particles that move slowly and interact only gravitationally with other particles. The competing view is the hot dark matter (HDM) model which considers dark matter particles moving at relativistic speeds, making it hard for particles to clump together and form structures. Models of structure formation incorporating cold dark matter are favored (e.g. Carroll and Ostlie 2007). In the CDM model structures form and grow in a bottom up 'hierarchical' way. In this theory, primordial perturbations grow, due to their self gravity, forming small structures which then collectively combine to form the large observed structures (Peacock 2007, Lacy and Cole 1993). This scenario is supported by various high redshift observations in the sense that galaxies at high redshifts are smaller than those in today's Universe.

Studying galaxy formation and evolution is an important part of studying the evolution of structure. Galactic evolution depends strongly on how fast the gas in the ISM is converted into stars. As molecular clouds get dense and collapse under their own gravity, they form dense cores that continue to accrete matter while forming stars. Knowing that galaxy evolution is limited to Gyr timescales, the study of galaxy evolution in simulated models is a major goal of computational cosmologists. When modeling galaxies, star formation is an essential process that must be included. Star formation is a major component of galaxy evolution models both through the formation of stars and also the so-called feedback processes (heating the ISM from supernovae and winds). Modeling star formation from first principles is not possible in simulations of galaxy formation. The lack of understanding of how the physics controlling star formation can be implemented on large scales poses a major challenge when modeling star formation in cosmological simulations.

In this thesis, we study the effect different star formation algorithms have on the morphology of galactic disc models in an attempt to better understand how the small scale physics governing star formation extends to large scales. This thesis will be a stepping stone for research on the effect of star formation algorithms on structure in cosmological simulations. Galactic disc models with different star formation algorithms were simulated. The morphologies of the discs were analyzed and compared in order to study the effect of the algorithms on the morphology of the disc models.

The structure of this thesis is as follows: In Chapter 2 a summary of theoretical and observational results is presented to provide additional background. In Chapter 3 the primary computational astrophysics methods, namely n-body and smoothed

particle hydrodynamics, are introduced. The simulation code is also discussed in detail here. We then follow with an overview of the simulation models in Chapter 4. In Chapter 5 results are presented along with a discussion of their implications. We conclude in Chapter 6 with a brief summary and suggest future work.

Chapter 2

Theory and Observational Background

2.1 Structure Formation

'How did the Universe become what we see today? How did this structure form? How does it evolve?' These are major questions that have been asked since the earliest days of astronomy. The field of Cosmology allows astronomers to better understand the early Universe, its formation, and evolution to the modern universe we observe today. Modern observations reveal a Universe that is populated with structures varying from planets, stars, star clusters, galaxies of different types and forms, clusters of galaxies, and even superclusters of galaxies. . . A variety of observational evidence suggest these structures evolved from a hot dense nearly uniform early Universe. It is thus necessary to model the early Universe before trying to understand how structure forms and evolves.

2.1.1 Friedmann's Equation

Einstein's theory of general relativity plays an essential role in understanding the evolution of our universe. Consider Einstein's field equation:

$$\mathcal{G}_{\mu\nu} = -\frac{8\pi G}{c^4}\mathcal{T}_{\mu\nu} \tag{2.1}$$

G is Newton's gravitational constant, $\mathcal{T}$ is the stress-Energy tensor which evaluates the effect of a given mass-energy distribution on the nature of space time, and $\mathcal{G}$ is Einstein's gravity tensor.

By solving Einstein's field equation for an isotropic and homogeneous universe, we can describe the evolution of the universe with a differential equation know as the Friedmann's equation. Friedmann's equation relates the scale factor to the density and the geometry of the Universe. The equation generally has the following form (e.g. Carroll and Ostlie 2007):

$$[(\frac{1}{R}\frac{dR}{dt})^2 - \frac{8}{3}\pi G\rho]R^2 = -kc^2 \tag{2.2}$$

R is the scale factor of the Universe, ρ is the cumulative density contribution of matter, radiation and vacuum $\rho = \rho_m + \rho_r + \rho_\Lambda$. k is a parameter describing the geometry of the universe (which can take values of 1, 0, or -1 corresponding to a closed, flat or open universe respectively). We can define a critical density ρ_c for which k = 0 such that:

$$\rho_c = \frac{3H^2}{8\pi G} \tag{2.3}$$

Introducing the critical density and the Hubble constant, H, Friedmann's equation can then be rearranged and written in a unit-less form:

$$H^2[1 - (\Omega_m + \Omega_r + \Omega_\Lambda)]R^2 = -kc^2 \tag{2.4}$$

where Ω is the dimensionless density defined as $\Omega_n = \rho_n/\rho_c$. Different combinations of density and pressure physics lead to different cosmological models that have their own expansion behaviors versus time.

2.1.2 Einstein de Sitter Model

Einstein and de Sitter contributed to the understanding of the early Universe by proposing a cosmological model in 1917. This model is known as the Einstein de Sitter model of the early universe. The Einstein de Sitter model assumes a spatially flat universe, and that the energy density is dominated by matter. It therefore satisfies Friedmann's equation assuming the following values of k, ρ_m, ρ_r, and ρ_Λ:

$$k = 0, \rho_m = 1, \rho_r = \rho_\Lambda = 0$$

From this cosmological model, we can begin to build an understanding of how structure evolved in the universe[1]. Note that we do not live in an Einstein de Sitter Universe, in-fact, we live in a Friedmann-Lemaître Universe which can be reduced to an Einstein de Sitter Universe by ignoring the cosmological constant

[1]The Einstein de Sitter model is a useful model for theoretical exploration because it predicts very simple solutions for the evolution of the scale factor with time, namely $a(t) \propto t^{2/3}$

2.1.3 From Perturbation to Structure

Although it was nearly uniform, the early Universe was not perfectly homogeneous; it was populated with small perturbations. These perturbations can be described statistically by a Gaussian random field, which theoretical models show could have given rise to today's large structures. The early Universe's inhomogeneities are observed in the Cosmic Microwave Background Radiation (CMBR) maps. Various studies examined the growth of such perturbations. White (1993) gives a linear perturbation theory derivation that shows how slight density perturbations (only in an Einstein de Sitter Universe) are amplified in proportion to the scale factor, and can grow to become large structures. Perturbations in a Universe other than the Einstein de Sitter Universe grow at different rates.

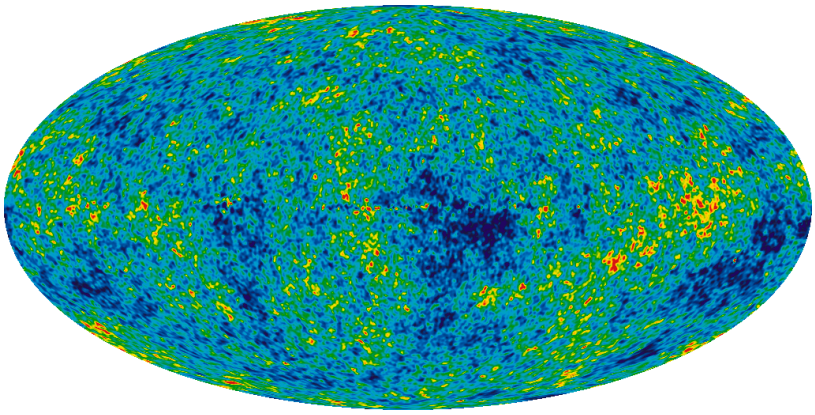

Figure 2.1: Simulated WMAP Cosmic Microwave Background (CMB) map showing the slight inhomogeneity of the early universe represented as small perturbations at the last scattering surface (NASA/WMAP Science team, WMAP # 121238).

Because the first structures to form in this model of structure formation are the smallest, the leading model in explaining structure formation is the bottom-up hierarchical structure formation model. This is the natural outcome of the Cold Dark

Matter (CDM) Model of the Universe. Cold dark matter is a form of matter that only interacts with baryonic matter gravitationally. CDM has a major contribution to the total energy density of the Universe which is represented by the term Ω_m in equation 2.4. Because of its slow motion ($v_{DM} \sim$ small fractions of the speed of light), CDM can easily accumulate under self gravity. In a CDM Universe smaller densities assemble together to form larger structures; this is depicted by a 'merger tree' (Lacey and Cole 1993). Baryonic matter is expected to behave similarly. The bottom-up structure formation model and the hierarchical evolution of structure is illustrated by Lacey and Cole (1993).

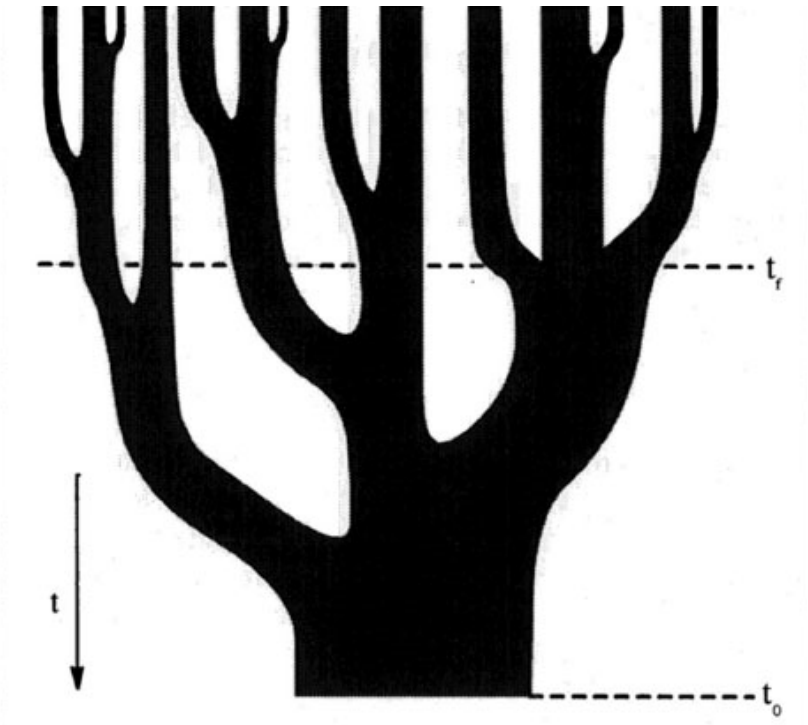

Figure 2.2: A schematic representation of a 'merger tree' depicting the growth of a halo (used with permission of C. Lacey).

Understanding how perturbations or halos form and evolve into more complex structures is one of the most essential concepts in understanding the evolution of the

universe. Knowing that structure on large scales is affected by small scale structure, We will need to know more about both to have a complete understanding of structure formation.

2.2 Star Formation

Galaxy evolution depends on how fast a galaxy's interstellar gas is converted into stars. Therefore, understanding star formation and its effect on the galaxy is a key to better understanding galaxy evolution. We choose to examine galaxy formation and evolution to enhance our knowledge of structure formation and evolution in astrophysical simulations, and therefore understanding how the complex and structured Universe that we observe today formed from an almost homogeneous Universe.

It may be useful to consider different mechanisms that facilitate star formation in galaxies according to the scales at which they occur. One can roughly break the process down into the following three major stages in disc galaxies: (1) The creation of the galactic arms, (2) the formation of molecular clouds, (3) the collapse of molecular clouds, and formation of dense cores. (1) and (2) are related to the large scale evolution in the galaxy, and it is worth noting that spiral arms are not needed to have Giant Molecular Clouds (GMCs) form. Knowing that we are interested in modeling star formation in large scale simulations, understanding star formation on small scales (stage 3) is very important.

2.2.1 Star formation Criteria

Stars form in the densest parts of the interstellar medium (ISM) known as molecular clouds (Larson 2003). Galactic spiral arm segments, containing molecular gas (Solomon and Sanders 1985, Elmegreen 1985, 1993), contain several Giant Molecular Clouds (GMCs). GMCs have sizes up to 100pc and masses up to $10^6 M_\odot$, which usually contain smaller scale clumpy structures (Blitz 1993, Blitz and Williams 1999, Williams et al 2000). In order to understand the collapse of these clumpy structures, also known as cores and globules, we can consider the forces affecting the collapse. Those forces can be grouped into the following main categories: (1) gravity, (2) gas and radiation pressure, (3) magnetic fields, and (4) the collective motion of the cloud and galactic shear. The first force is the one responsible for the collapse, while the remaining forces act as sources of support against the collapse. Ignoring rotation, turbulence, and magnetic fields, one can simplify the collapse of cores and globules in molecular clouds. This makes it possible to derive a minimum mass criterion for which cores and globules can collapse under their own gravity.

Mass Criterion

Sir James Jeans (1902) studied the effect of slight fluctuations from the hydrostatic equilibrium on a stable gravitationally bound system. Such a system, when at equilibrium, can be described by the virial theorem (equation 2.5)

$$2K + U = 0 \tag{2.5}$$

where K is the kinetic energy and U is the potential energy of the system. Assuming a spherical cloud of constant density, the gravitational potential energy and the internal kinetic energy of the cloud are given by:

$$U \simeq -\frac{3}{5}\frac{G{M_c}^2}{R_c}$$
$$K = \frac{3}{2}\frac{M_c kT}{\mu m_H} \tag{2.6}$$

where M_c and R_c are the mass and radius of the cloud respectively, G is the gravitational constant, μ is the mean molecular weight, m_H is the mass of hydrogen, T is the temperature, and k is Boltzmann's constant.

For the cloud to collapse, the absolute value of the gravitational potential energy must exceed twice the kinetic energy of the cloud. Using this collapse criterion, equation 2.6, and substituting $R_c = (\frac{3M_c}{4\pi\rho_0})^{1/3}$ where ρ_0 is the initial density of the cloud, one can derive a condition on the minimum mass necessary to initiate a spontaneous cloud collapse. This criteria is known as the Jeans criterion:

$$M_c > M_J \tag{2.7}$$

where M_J is the Jeans mass, and it can be expressed as follows:

$$M_J \simeq (\frac{5kT}{G\mu m_H})^{3/2}(\frac{3}{4\pi\rho_0})^{1/2} \tag{2.8}$$

This derivation of the Jeans mass neglected any external pressure exerted on the core or the cloud by the interstellar medium (ISM). The critical mass required to initiate gravitational collapse in the presence of an external pressure (P_0) is given by the Bonnor-Ebert mass:

$$M_{BE} = \frac{c_{BE} {v_T}^4}{{P_0}^{1/2} G^{3/2}} \tag{2.9}$$

where $v_T = \sqrt{\frac{kT}{\mu m_H}}$ is the isothermal sound speed, and c_{BE} is a dimensionless constant given by $c_{BE} = 1.18$.

Temperature and Density Criteria

Using the equation for the Jean's mass, one can deduce criteria that minimize the Jean's mass and thus play an important role in star formation and the collapse of clouds. Knowing that the the Jean's mass (M_J)scales as $T^{3/2}$ and ${\rho_0}^{-1/2}$, one would expect stars to form in regions of dense and cool gas. Stars are known to form in regions where (i.e. Thacker and Couchman 2000, Wurster and Thacker 2013):

1. The gas is dense (density exceeds 0.01cm^{-3})
2. The gas cool (temperature less than $3 \times 10^4\text{K}$)
3. Baryonic matter is partially self-gravitating ($\rho_{gas} > 0.4\rho_{DM}$)
4. The flow is convergent ($\nabla \cdot \vec{v} < 0$)

2.2.2 Star Formation Rates

The main reason for studying star formation in this thesis is our interest in its effects on the galaxy's evolution and morphology. As mentioned before, galactic evolution is governed by how fast the the galactic gas reservoir is converted into stars. Therefore, examining the star formation rate (SFR) is a reasonable approach to quantitatively study star formation, and hence galactic evolution.

Although different disc galaxies seem to exhibit wide variety of star formation rates, they appear to follow two empirical laws (Li et al 2006). The first law is the star formation threshold, where efficient star formation occurs for densities higher than a critical surface density (Martin and Kennicutt 2001). The second law is the Schmidt law (Schmidt 1959). Introduced by Schmidt in 1959, the Schmidt law implemented a power law correlation between the SFR surface density and the gas surface density. The Schmidt law has the following format:

$$\Sigma_{SFR} = A{\Sigma_{gas}}^{N} \tag{2.10}$$

where Σ_{SFR} and Σ_{gas} are the surface densities of SFR and the gas respectively, A is a normalization coefficient, and N is the star formation index. Kennicutt (1998) presented a star formation index $N = 1.4 \pm 0.15$, providing an excellent model of star formation over several orders of magnitude in SFR and gas surface densities.

The Schmidt law is considered a useful way of modeling the SFR in numerical simulations of galaxy formation and evolution. Knowing that computational efficiency is a valuable commodity in computational science, a Lagrangian form of the Schmidt

law, based upon mass rather than density, can be used as shown in equation 2.11. This version corresponds to a star formation index $N = 1.5$ (Thacker and Couchman 2000, Katz 1992) and can be expressed as:

$$\dot{M}_* = C_{sfr} {\rho_g}^{1/2} M_g \tag{2.11}$$

where C_{sfr} is the star formation rate normalization, and the subscripts g and $*$ correspond to gas and stars respectively.

2.3 Theoretical Considerations Compared to Observations

Computational astrophysicists must develop models that are consistent with observations. These observations, are often of a smaller size or scale than the minimum allowed resolution in the simulations. This is a fact that plays an important role in simulations of galaxy formation and evolution and has been called 'The Scale Challenge'. Simulations of galaxy formation and evolution must take into account studies of the star forming regions of galaxies, but inevitably, star forming regions fall below the minimum resolution in such simulations. This is illustrated by Nguyen Luong et al (2011) (see figure 2.3).

Nguyen Luong et al (2011) investigated star formation in the infrared dark cloud (IRDC) filament G035.39-00.33 in the W48 molecular cloud complex (Rygl et al 2010). They used data from the PACS and SPIRE cameras of the Herschel space observatory.

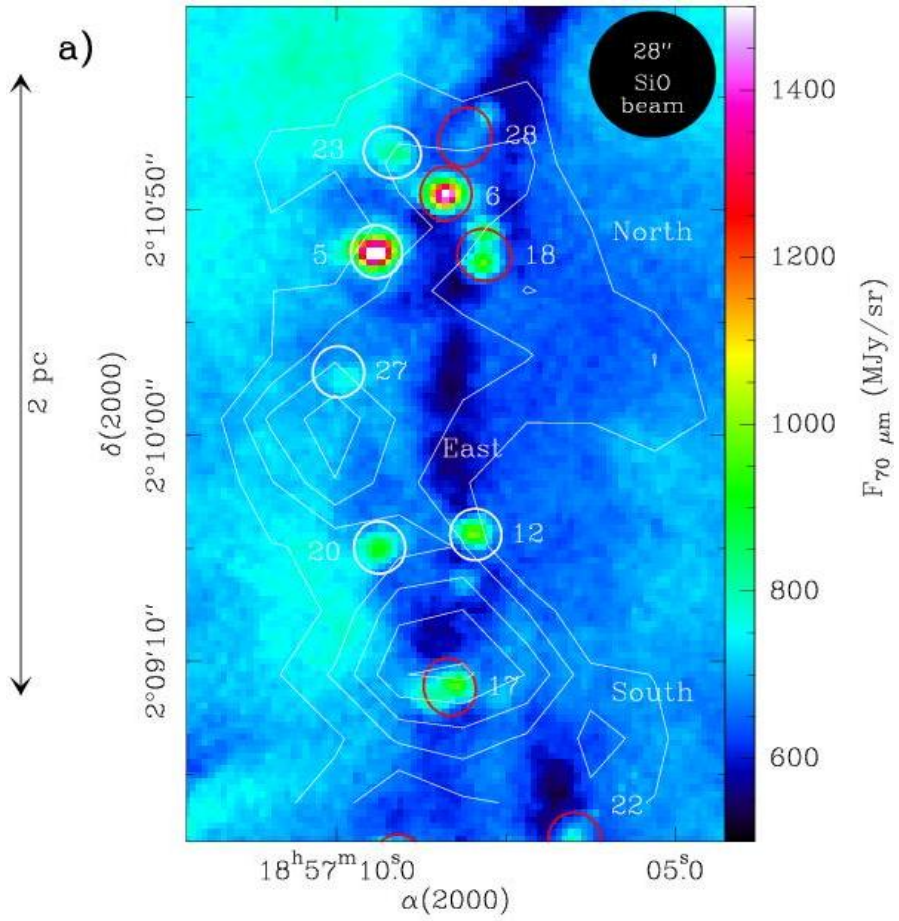

Figure 2.3: Part of G035.39-00.33 seen at 70μm. The dense cores with mass $> 20M_{\odot}$ are indicated by red ellipses, those with mass $< 20M_{\odot}$ by white ellipses. The contours indicate SiO emission, and the color map is a plot of the flux measured.(used with permission of Q. Nguyen Luong.)

The W48 molecular cloud complex is one the regions forming high-mass stars within 3kpc from the sun. The G035.39-00.33 has an effective mass of approximately 9000 $M_{\odot}$ and an effective radius of 10pc (Simon et al 2006). Nguyen Luong et al found that among the total of 28 dense cores detected by Herschel, which had a spectral energy distribution (SED) FWHM of approximately 0.15pc, 13 massive dense cores (MDCs) are potentially forming high mass stars. Figure 2.3, illustrates the relative small sizes of MDCs exhibiting star formation activity with respect to the host cloud.

According to the data presented by Nguyen Luong et al (2011), one may question whether the collapse of a region is critical when deciding on star formation criteria in galactic simulations. Since the star forming regions are smaller than 2pc and they have SED FWHM of approximately 0.15pc, the significance of the collapse condition ($\nabla \cdot \vec{v} < 0$) in galaxy formation simulations is debatable. Such simulations usually have resolutions that are orders of magnitude higher than the desired resolution of the collapsing cores.

Difficulties in modeling star formation in large scale simulations

Large scale models are often motivated by small scale physics. This may not always be done in the correct fashion. For example, although the concepts of pressure and temperature in gases are related to the kinetic theory of atomic collisions, we do not model gases on large scales by considering an ensemble of atoms colliding on small scales. Instead we rely upon hydrodynamics. This can be extended to modeling star formation on large scales. However, we do not understand how the small scale physics manifests on large scales which makes it difficult to model star formation on large scales. Many theories of the interstellar medium (ISM) have been proposed (ie. McKee and Ostriker 1977), yet there is no full understanding of the ISM.

Chapter 3

Computational Methods

3.1 Nbody

N-Body methods are used to simulate dynamical systems of particles to study the non linear processes of structure formation (Hockney and Eastwood 1988). The N-Body method is a Lagrangian method which represents a collisionless fluid as an ensemble of discreet particles to which certain attributes are assigned. These attributes (such as mass, density, position, velocity) evolve according to the equations of motion which are in turn governed by the field equations. The most important of all field equations (for a gravitational N-Body problem) is Poisson's equation for a gravitational field,

$$\nabla^2\phi = -4\pi G\rho \tag{3.1}$$

where ϕ is the scalar potential, and ρ is the density. Equation 3.1 can be derived from Gauss's law of gravity by substituting $\mathbf{g} = -\nabla\phi$ into the differential form of Gauss's law,

$$\nabla \cdot \mathbf{g} = -4\pi G\rho \tag{3.2}$$

Different particle simulations use different methods of solving the corresponding field equation which is usually an elliptic partial differential equation.

Overall, an N-Body method defines a system by its initial conditions (e.g. initial values), equations of motion that are determined by the field equations, and the boundary conditions which define the external forces on the system as well as the volume in space that the particles are allowed to exist in. With these three criteria, the description of an N-Body system is complete.

3.1.1 Benefits of Lagrangian Methods

In order to model a fluid, we define a fixed coordinate system, and we describe variables as functions of $(\mathbf{r}, t)$. Describing the change of a variable from the point of view of a fixed point in space is known as the Eulerian reference frame (fixed grid). In computational simulations, this approach is known to be effective in modeling shocks and magnetic fields. Modeling several orders of magnitude in resolution proposes a challenge to the Eulerian approach. On the other hand, describing the change of variables from the point of view of fluid elements that are considered to be stationary with respect to the coordinate system is known as the Lagrangian frame of reference. Lagrangian computational methods have the advantage of resolving several orders of magnitude because resolution elements move with the flow.

In a Eulerian reference frame, derivatives are the sum of partial time and space derivatives. On the contrary, in Lagrangian reference frames, properties of a fluid element are determined as a function of the element's initial position. Therefore the location of a fluid element (spatial dependency) is dependent on time. Thus, the derivatives, in a Lagrangian reference frame, are the convective derivative (all spatial

and time variables are a function of time). The convective or Lagrangian derivative can be expressed as:

$$\frac{D}{Dt} = \frac{\partial}{\partial t} + \mathbf{u} \cdot \nabla \tag{3.3}$$

where $\mathbf{u} = \frac{\partial \mathbf{r}}{\partial t}$ is the velocity of the fluid.

3.1.2 Particle Models

To solve an N-Body problem, there are various types of particle simulation models that can be used, of which we will mention the following (Hockney and Eastwood 1988):

1. Particle-particle (PP) models: This model considers the forces acting on a system from a distance (e.g. Gravity, Coulomb force) by directly calculating forces through pairwise interaction (N^2 interactions are considered). Because of the intensive computations required, this model is slow for high resolutions.

2. Particle-mesh (PM) model: This model approaches the forces as field quantities that is then approximated on a mesh (grid). The gravitational potential of the system is constructed over a grid starting from the density field and by solving the associated Poisson equation. The resolution of this method is determined by the spacing of the mesh. This is a low resolution method.

3. Particle-particle-particle-mesh (P^3M) model: This model is a combination of both the PP and the PM methods, and therefore it combines both of their advantages. It is accurate at representing close encounters (PP method) and

allows rapid calculations of long-range forces (PM method). This method is computationally efficient and allows high resolution. A major disadvantage of this method is its vulnerability to clustering in high density regions, i.e. the algorithm can slow down significantly.

4. Adaptive P^3M (AP^3M) model: This model uses an adaptive sub-grids rather than a static grid, therefore more grid elements are concentrated where a higher resolution is needed (regions of higher densities). This feature remedies the slow-down due to clustering in high density regions.

3.2 SPH

The Smoothed Particle Hydrodynamics (SPH) method is a particle method that was initially introduced to simulate nonaxisymmetric phenomena in astrophysics such as collisions of gas clouds (Gingold and Monaghan 1977, Lucy 1977). Since its invention, SPH has become widely applied and it is now applied to diverse astrophysical problems from radio jet simulations, to simulations of motion near black holes (Monaghan 1992). The main reasons for the popularity of SPH is how easy it is to work with, the reasonable and accurate results it leads to in difficult situations, and its ability to handle complex physics in three dimensional problems with ease (Monaghan 1992). This popularity can also be related to SPH being a Lagrangian method which gives it several advantages over Eulerian methods such as calculations in high density regions.

3.2.1 THE HEART OF SPH

SPH is based on interpolating functions, that allow field quantities to be interpolated anywhere from a set of points representing the particles (Gingold and Monaghan 1977, 1982, Lucy 1977). Any function $A(\mathbf{r})$ is expressed in terms of its integral interpolant $A_I(\mathbf{r})$ which is given by:

$$A_I(\mathbf{r}) = \int A(\mathbf{r}')W(\mathbf{r}-\mathbf{r}', h)d^3\mathbf{r}' \tag{3.4}$$

where W is an interpolating kernel (see below), and h is the smoothing length; it determines the size of the smoothing region. The interpolating kernel must mimic a delta function as $h \to 0$ and must thus have the following properties:

$$\begin{gathered}\int W(\mathbf{r}-\mathbf{r}', h)d^3\mathbf{r}' = 1 \\ \lim_{h\to 0} W(\mathbf{r}-\mathbf{r}', h) = \delta(\mathbf{r}-\mathbf{r}')\end{gathered} \tag{3.5}$$

Other kernels can be designed (see Natanson 1960, Monaghan 1982). One famous example would be the kernel based on spline functions (Monaghan and Lattanzio 1985) which is given by:

$$W(\mathbf{r}, h) = \frac{\sigma}{h^\nu}\begin{cases} 1 - \dfrac{3}{2}q^2 + \dfrac{3}{4}q^3 & \text{if } 0 \le \frac{r}{h} \le 1; \\ \dfrac{1}{4}(2-q)^3 & \text{if } 1 \le \frac{r}{h} \le 2; \\ 0 & \text{otherwise.} \end{cases} \tag{3.6}$$

where ν is the number of dimensions and σ is a normalization constant with the values $\frac{2}{3}$, $\frac{10}{7\pi}$, and $\frac{1}{\pi}$ corresponding to one, two and three dimensions respectively.

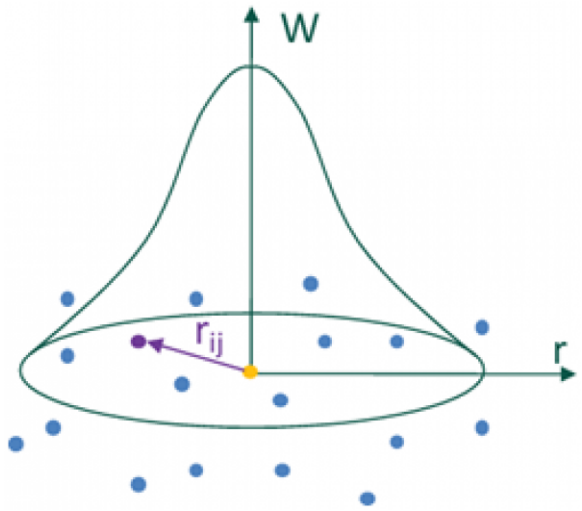

Figure 3.1: A schematic drawing depicting the heart of SPH by showing a function expressed in terms of its interpolating kernel (in 2D) smoothed over its neighboring particles (Komoroczi et al 2013, used with permission of A. Komoroczi) .

When using the integral interpolant shown in equation 3.4 in numerical simulations, the integration is approximated by a summation interpolant $A_S(\mathbf{r})$ which is effectively a mass-weighted sum over N neighboring particles and may be expressed as:

$$A_S(\mathbf{r}) = \sum_b^N m_b \frac{A_b}{\rho_b} W(\mathbf{r} - \mathbf{r}_b, h) \tag{3.7}$$

where the summation iterates over all particles labeled by b. A particle n will have mass m_n, position $\mathbf{r}_n$, velocity $\mathbf{v}_n$, and density ρ_n. Therefore, any function or field $A(\mathbf{r})$ can be smoothed and estimated as a weighted summation over particles using equation 3.7. Derivatives can be calculated using ordinary differentiation as shown

below.

$$\nabla A(\mathbf{r}) = \sum_{b}^{N} m_b \frac{A_b}{\rho_b} \nabla W(\mathbf{r} - \mathbf{r}_b, h) \tag{3.8}$$

SPH does not need a grid to calculate spatial derivatives. In SPH, derivatives of interpolants can be obtained by ordinary differentiation of the kernel. Therefore, the equations governing energy and momentum are a set of differential equations that are easy to derive and manipulate.

3.2.2 The Nearest Neighboring Particle

The basis of SPH is interpolating field quantities from a set of neighboring points (particles). In simulations, before SPH can be implemented, one needs to decide what region a function is being smoothed over. In other words, we need to decide what points (particles) are to be used when interpolating the field quantities. To choose these points, the Nearest Neighboring Particle (NNP) method is used. The NNP concept can be interpreted differently leading to different meanings of the smoothing length h (Hernquist and Katz 1989, Shapiro et al 1996, Liu et al 2003, Di Blasi et al 2011).

In the first approach, known as the 'gather' approach, h is considered the radius of the smoothing kernel of particle t at $\mathbf{r}$. Only particles inside the radius h will be considered as NNPs of$t$ when implementing SPH. The second approach, known as the 'scatter' approach, h_b is considered the radius of the smoothing kernel of a particle t_b at $\mathbf{r_b}$. Particle t_b will be considered as a NNP of t only if $|\mathbf{r} - \mathbf{r_b}| < h_b$. When using the 'gather' approach, equation 3.7 remains unchanged. While when using using the

'scatter' approach, the interpolating kernel $W(\mathbf{r} - \mathbf{r_b}, h)$ in equation 3.7 is expressed as $W(\mathbf{r} - \mathbf{r_b}, h_b)$. Figure 3.2 demonstrates the differences between the 'gather' and 'scatter' approaches.

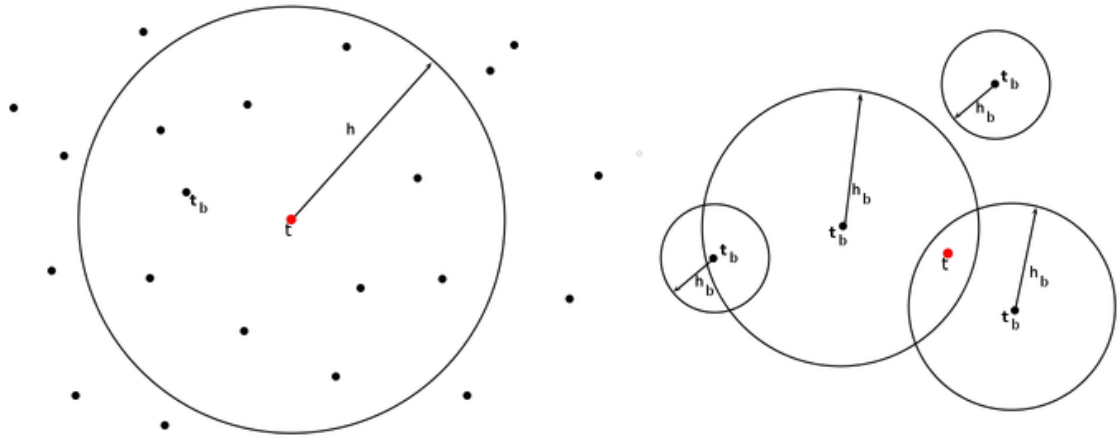

Figure 3.2: A schematic drawing depicting the NNP (t_b) for particle t using the two different approaches: the gather approach (left), the scatter approach (right).

3.3 HYDRA

HYDRA is a SPH AP^{3}M code developed by Couchman, Thomas and Pearce in 1995, which simulates cosmological hydrodynamics. It is written in FORTRAN77. The version of HYDRA we will discuss in this section (HYDRA_OMP) is the parallel version developed by Thacker and Couchman (2006). HYDRA_OMP is written in FORTRAN77 and OpenMP. The use of OpenMP API for multi-platform shared-memory programming allows loop level parallelism (Thacker and Couchman 2006).

3.3.1 Why Parallel Computing?

Our interest in parallel computing, similar to other computational cosmologists' interest, branches from two major reasons (Thacker and Couchman 2006): (1) the desire of higher resolutions, and (2) our interest in completing the simulations in the shortest time frames[1]. There are two issues that promote a need for progressively higher resolution. Firstly, cosmological simulations' aim is to make statistical predictions, therefore it is important to have a high simulation volume in order to insure a low sample variance. Secondly, simulating structure formation and evolution requires high mass resolution which is solely due to the hierarchical model of structure formation and growth in a CDM Cosmology.

3.3.2 Structure of the HYDRA code

The Time Integrator

At the heart of HYDRA is a single-step predictor-corrector type integrator (Couchman, Thomas and Pearce 1995). This integrator calculates the forces once per step at a predicted position $\mathbf{r}'$. Using this force along with the force from the step before, the position and velocities are corrected as described by Couchman, Thomas and Pearce

[1]Thacker and Couchman (2006) studied the speed-up produced by the parallelization of HYDRA using a 64 processor SGI Origin 3000, and a 64 processor Hewlett Packard GS1280. Simulating 2×256^3 particles with a 512^3 mesh and 64 parallel execution threads, HYDRA_OMP was found to be 59.8 times faster than HYDRA when running on the SGI Origin 3000, and 56.6 times faster when using HP GS1280.

(1995):

$$\mathbf{r}_{n+1} = \mathbf{r}_n + \mathbf{v}_n dt + [(1-\alpha)\mathbf{f}(\mathbf{r'}_n) + \alpha\mathbf{f}(\mathbf{r'}_{n+1})]dt^2/2$$

$$\mathbf{v}_{n+1} = \mathbf{v}_n + [(1-\beta)\mathbf{f}(\mathbf{r'}_n) + \beta\mathbf{f}(\mathbf{r'}_{n+1})]dt \tag{3.9}$$

where

$$\mathbf{r'}_{n+1} = \mathbf{r}_n + \mathbf{v}_n dt + \mathbf{f}(\mathbf{r'}_n)dt^2/2 \tag{3.10}$$

This integrator is equivalent to a Leapfrog integrator for velocity-independent forces.

The Gravitational Solver

To use the integrator discussed above, the gravitational forces need to be calculated. The gravitational forces can be expressed as a sum of two separate terms:

$$\mathbf{F}_{grav} = \mathbf{F}_{short} + \mathbf{F}_{long} \tag{3.11}$$

where $\mathbf{F}_{long}$ is a long range force that can be determined using a Fourier-based solver using the Particle-Mesh aspect of the code. On the other hand, $\mathbf{F}_{short}$ is the short range force determined by iterating a sum over neighboring particles within a short range radius, using the Particle-Particle aspect of the code. $\mathbf{F}_{long}$ can be smoothed over the mesh to increase the accuracy of $\mathbf{F}_{grav}$. In case of clustering of particles, the AP^{3}M method isolates such regions onto a sub-grid preventing a slow-down.

The SPH Solver

For the SPH, an explicit 'gather' smoothing kernel is used. The average of the kernel W, in equation 3.8, is used to ensure the replacement (equation 3.12) is correct to $O(h)$. Therefore, the following substitution is made:

$$\nabla_j \bar{W}(\mathbf{r}_i - \mathbf{r}_j, h_j, h_i) = -\nabla_i \bar{W}(\mathbf{r}_i - \mathbf{r}_j, h_i, h_j) + O(\nabla h) \tag{3.12}$$

Equation Sets

Knowing that the simulation of structure formation and evolution is an initial value problem, HYDRA uses a set of initial conditions and then solves the following gravito-hydrodynamic equations;

(1) the continuity equations which are satisfied by the use or a particle based method,

$$\begin{aligned} \frac{d\rho_g}{dt} + \rho_g \nabla \cdot \mathbf{v}_g = 0 \\ \\ \frac{d\rho_{dm}}{dt} + \rho_{dm} \nabla \cdot \mathbf{v}_{dm} = 0 \end{aligned} \tag{3.13}$$

where the subscripts g and dm denote gas and dark matter respectively,

(2) the Euler and acceleration equations,

$$\begin{aligned} \frac{dv_g}{dt} = \frac{1}{\rho_g} \nabla P - \nabla \phi \\ \\ \frac{d\mathbf{v}_{dm}}{dt} = -\nabla \phi \end{aligned} \tag{3.14}$$

(3) the Poisson equation,

$$\nabla^2\phi = 4\pi G(\rho_g + \rho_{dm}) \tag{3.15}$$

(4) the entropy conservation equation or the conservation of energy equation,

$$\begin{aligned} \frac{ds}{dt} &= 0 \\ \\ \frac{du}{dt} &= -\frac{P}{\rho_g}\nabla \cdot \mathbf{v}_g \end{aligned} \tag{3.16}$$

3.3.3 HYDRA IN A NUTSHELL

Finally, as a brief panorama of HYDRA, I present the solution cycle of a single time-step as summarized in TC06 :

1. Assign mass to the Fourier mesh.

2. Convolve with the Green's function using the FFT method to get potential. Difference this to recover mesh forces in each dimension.

3. Apply mesh force and accelerate particles.

4. Decide where it is more computationally efficient to solve via the further use of Fourier methods as opposed to short-range forces and, if so, place a new sub-mesh (refinement) there.

5. Accumulate the gas force (and state changes) as well as the short-range gravity for all positions not in sub-meshes.

6. Repeat (1)-(5) on all sub meshes until forces on all particles in simulation have been accumulated.

7. Update time-step and repeat.

It is worth noting that star and dark matter particles are handled the same way in HYDRA.

Chapter 4

Simulation Models

Thus far, we have been discussing the theory and methods used, but we did not consider the main focus of this research. Everything discussed up to this point can be applied to many classes of simulations dealing with structure, particularly galaxy, formation and evolution. It is now timely to more closely focus on the purpose of this thesis and the simulations carried.

4.1 The Simulations

We are interested in studying the effect of structure formation algorithms on the morphology and growth of structure. To do so, we started by examining the effects of different star formation algorithms on the star forming regions and therefore the morphology of isolated galactic disc models. Based on the debatable effect of the velocity divergence criterion for star formation, due to the limited resolution (see section 2.3), we ran four different low resolution simulations of isolated galactic discs and collapsing clouds. The initial conditions and other details of each simulation are discussed below (see sections 4.1.1 and 4.1.2).

Each simulation was performed on 32 cores (1 node) of the Cerberus cluster operated by the Institute of Computational Astrophysics (ICA) at Saint Mary's Uni-

versity[1]. Cerberus is a 304-core AMD Opteron processor cluster with an InfiniBand high-speed interconnect for MPI code. The simulations were run for a total of 369 hours of wall-clock time.

It is worth noting that we will be referring to the simulations which used the algorithm that limits star formation to collapsing regions only ($\nabla \cdot \vec{v} < 0$) as model-1, and the simulation which used the algorithm with no condition on $\nabla \cdot \vec{v}$ as model-2. A summary of the simulations is available in table 4.1.

4.1.1 Disc Simulations

Two simulations of isolated galactic discs were performed. Both simulations started with a disc distribution of 280,000 particles (100,000 dark matter particles, 100,000 stars, and 80,000 gas particles). One of the two simulations allowed star formation to occur only in collapsing regions ($\nabla \cdot \vec{v} < 0$), while the other had no conditions on $\nabla \cdot \vec{v}$. The simulations were allowed to run for ~ 1.02 Gyr, which amounts to ~ 5 rotations. Running for ~ 1.02 Gyr allowed the model to reach a less dramatic epoch of cloud and star formation (Williamson and Thacker 2012). Data outputs were written every 100 iterations. A softening length of 120pc was used which is large relative to the size of GMCs. Figure 4.1 shows z-projections of the two models at the initial and final times of the simulations.

[1]OpenMP API was used to parallelism

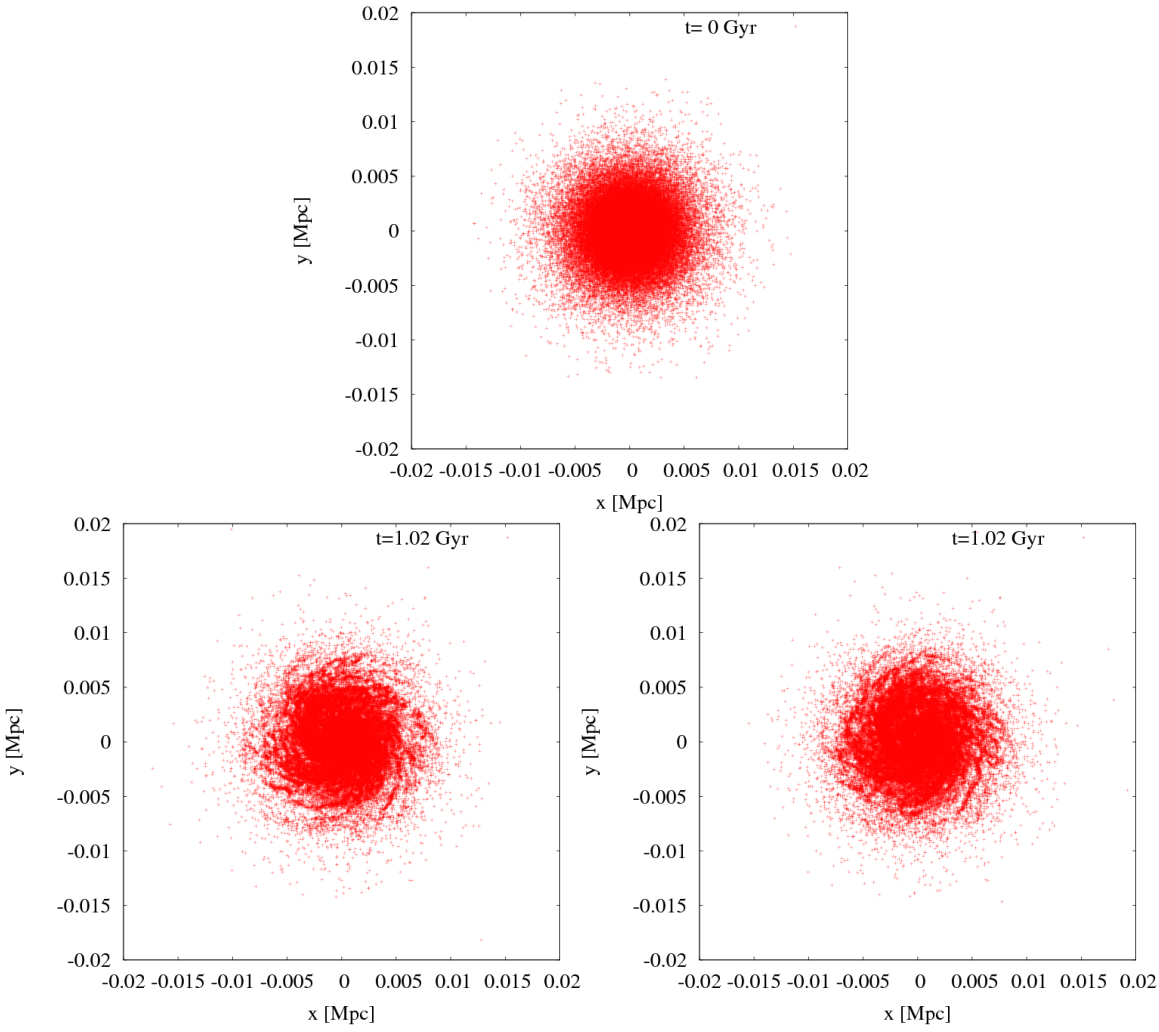

Figure 4.1: Gas particle plots of the two disc models at $t = 0$Gyr (top), and later in the simulation at $t = 1.02$Gyr (bottom). Model-1 (bottom left) shows some differences in the morphology when compared with model-2 (bottom right).

4.1.2 Cloud Collapse

Discs have a large sheering rotation. Hence, the $\nabla \cdot \vec{v} < 0$ condition is exclusive to small local high density regions. However, collapsing clouds have more complicated 3D velocities and more collapses on small scales which would show more obvious differences produced by the removal of the $\nabla \cdot \vec{v} < 0$ condition. We used the ΛCDM model which is considered a successful model for the formation of disc galaxies (Blu-

menthal et al 1984, Cole et al 1994, White and Rees 1978, Benson 2010). In a ΛCDM model, baryonic matter collapses inside a dark matter halo forming a galactic disc.

Two simulations of isolated collapsing clouds were performed. Each simulations started with a cloud of 100,000 particles (50,000 dark matter particles, no stars, and 50,000 gas particles); both clouds had a NFW profile (Navarro, Frenk and White 1996, 1997). An NFW profile is one of the most commonly used mass distributions of dark matter. The dark matter density can be expressed as a function of radius.

$$\frac{\rho(r)}{\rho_{crit}} = \frac{\delta_c}{\frac{r}{R_s}(1+\frac{r}{R_s})^2} \tag{4.1}$$

One of the two NFW cloud collapse simulations allowed star formation to occur only collapsing regions ($\nabla \cdot \vec{v} < 0$), while the other allowed star formation without any conditions on $\nabla \cdot \vec{v}$. The simulations were allowed to run for ~ 4.4 Gyr. Data outputs were written every 100 iterations. A softening length of 240pc was used. Note again that the softening length is large relative to the size of GMCs. Figure 4.2 and 4.3 shows the two models at the initial and final times of the simulations.

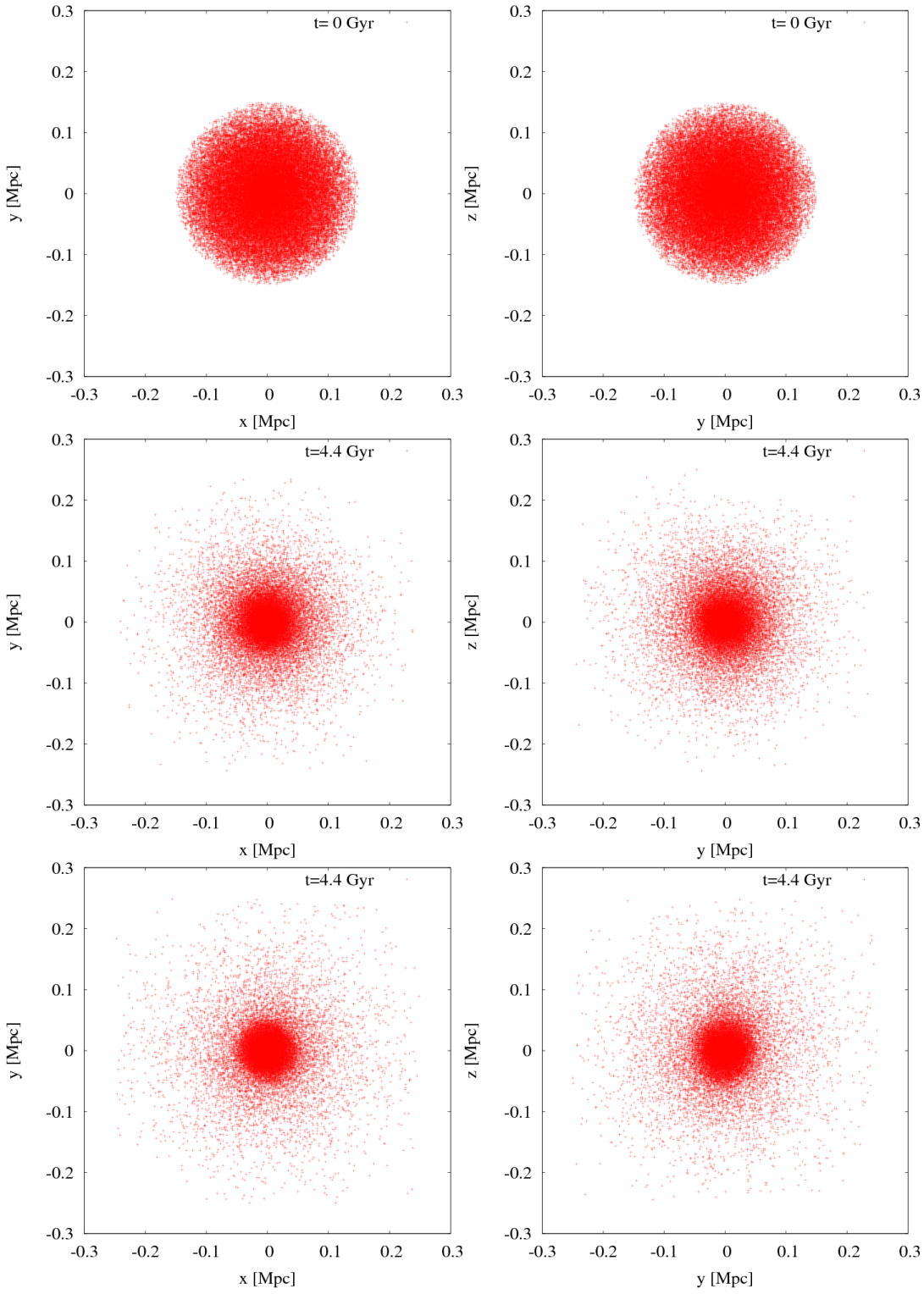

Figure 4.2: Gas particle plots of the two collapsed cloud models at $t = 0$Gyr (top) and $t = 4.4$Gyr, showing z (left) and x (right) projections. Model-1 (middle) shows evident differences in the morphology when compared with model-2 (bottom). Note that the disc structure is not visible in these plots as it is hidden by the particles around the galaxy.

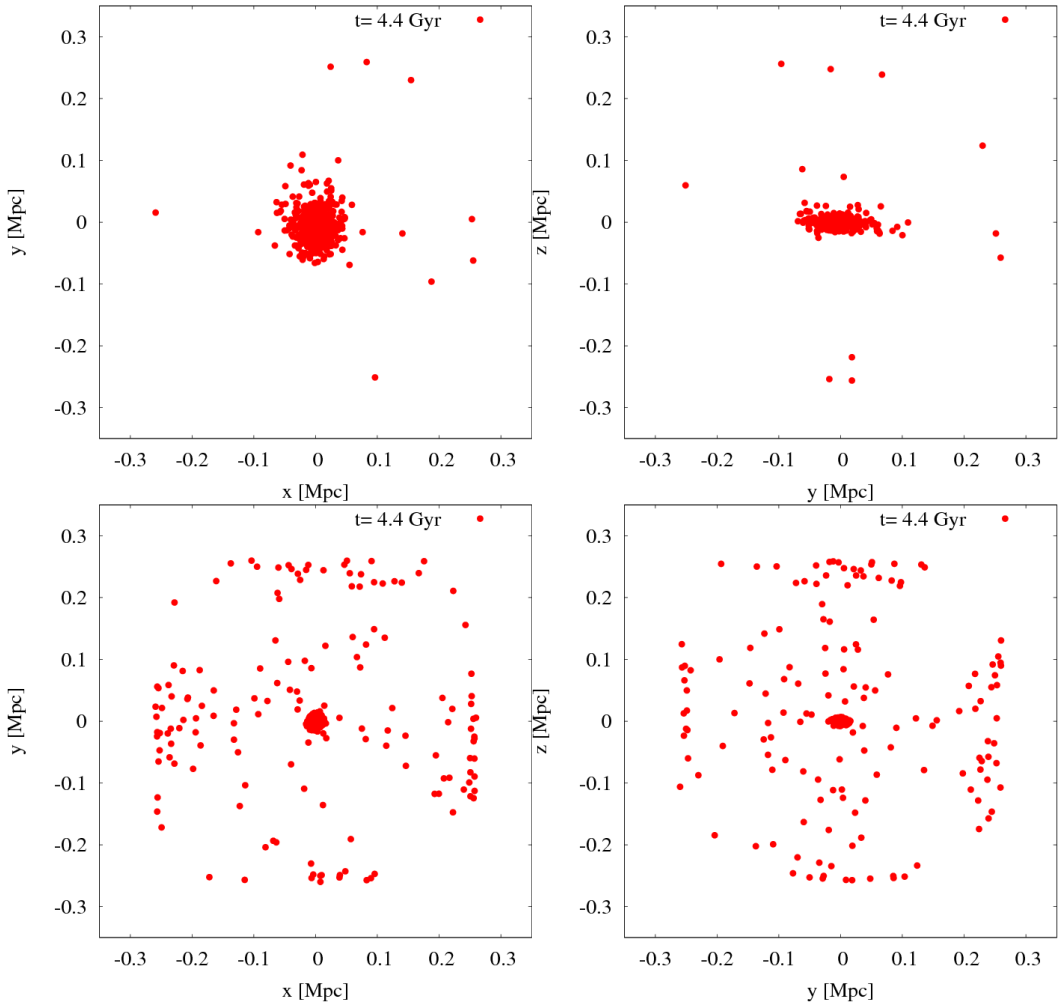

Figure 4.3: The star distribution in the two collapsed cloud models at $t = 4.4$Gyr showing z (left) and x (right) projections. Model-1 (top) shows evident differences in the morphology when compared with model-2 (bottom). The presence of a significant stellar population outside the disc plane could explain the diffuse hot halo in model-2 due to the feedback processes. Note the disc structure is evident in the z-y projections. The square pattern in the bottom panels is a relic of particles reaching the edge of computational domain.

Simulation	N_{dm}	N_{gas}	T_{evol} [Gyr]	IC type	$\nabla \cdot \vec{v}$	Softening length [pc]
DModel-1	100,000	80,000	1.02	D	on	120
DModel-2	100,000	80,000	1.02	D	off	120
CModel-1	50,000	50,000	4.4	CC	on	240
CModel-2	50,000	50,000	4.4	CC	off	240

Table 4.1: A summary of the conducted simulations.

4.2 Calibration

A major challenge facing every computational simulation is the calibration of the output data. Calibration is an essential tool in computational simulations as it helps validate the accuracy of the simulation and therefore the chosen models. Without calibration, it is unclear how well results map to physical models. In other words, calibration creates a reference basis for the results and facilitates comparison to observations. To make comparison against observational data possible, the star formation rates as well as various variables that are known to affect the star formation rates (such as temperature, density) were smoothed then plotted over the galactic disc; this is made possible by virtue of the SPH nature of the code.

One might naïvely think that the smoothing process will not change the SFR values. However, the smoothing changes the values of the smoothed quantity into volume density values; therefore, rather than plotting star formation rates the values plotted are star formation rate densities. Careful scaling must be followed to ensure the accuracy of the smoothing process. When plotting the star formation rates onto the grid, two major scaling issues arise, the resolution and the box size.

4.2.1 Resolution

The resolution of the plot is dictated by the number of cells the values are being smoothed over, with more cells obviously constituting a higher resolution. Consequently, as the resolution approaches a minimum (one cell), the star formation rate (SFR, Ψ_i) calculated for that single sell must equal the total star formation rate of

the galaxy (Ψ_{total}) (equation 4.2).

$$\lim_{i \to 1} \sum_{n=1}^{i} \Psi_n = \Psi_{total} \tag{4.2}$$

i in equation 4.2 corresponds to the number of pixels (or voxels in 3D).

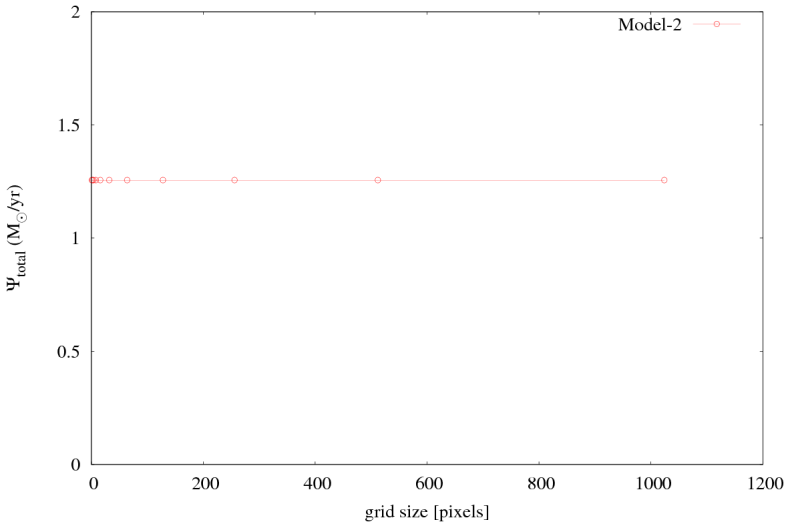

Figure 4.4: The variation in the resolution affects the SFR density, but not the total SFR. This plot shows that the total star formation rate is independent of the chosen resolution.

Since the total star formation rate is a property of the galaxy, it is evident that it should be independent of the resolution used. Figure 4.4 demonstrates the consistency of equation 4.3.

$$\sum_{i=1}^{npix} \Psi_i = \Psi_{total} \tag{4.3}$$

The smoothing as well as the scaling is dependent on the extent of the grid. It is expected that the extent of the grid, so long it is larger than the disc, should not have any effect on the total star formation rate. This is demonstrated in figure 4.5.

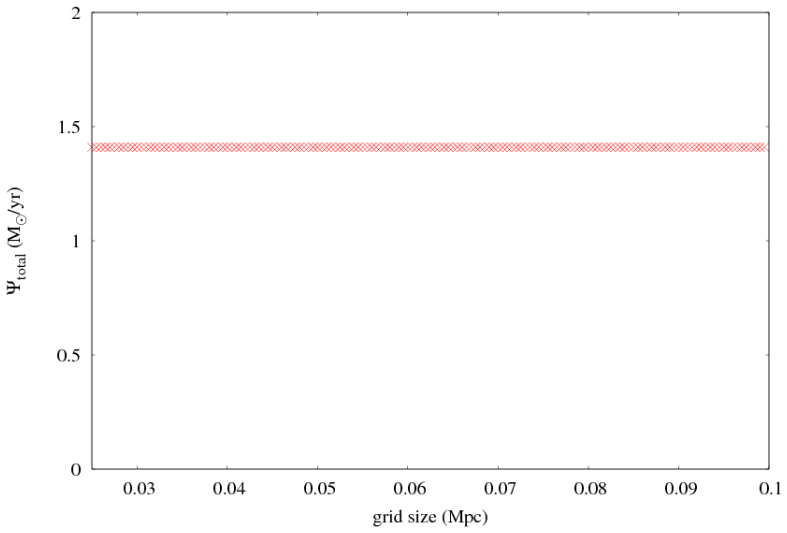

Figure 4.5: The variation in the grid size affects the SFR density, but not the total star formation rate in case of a grid size larger than the size of the galactic disc. This plot shows that the the total star formation rate is independent of the chosen grid size. The diameter of the disc is $\sim$ 25kpc.

4.2.2 Total SFR

An essential aspect of calibration is the comparison against observational data. A galactic disc similar to the Milky Way would be expected to have a total star formation rate ranging from 0.68 to 1.45$M_\odot$/yr (Robitaille and Whitney 2010). The disc simulations showed a total star formation rate converging to $\sim 1.25 - 3M_\odot$/yr after an initial high peak that is a product of the initial conditions (Williamson and Thacker 2012).

Chapter 5

Results and Discussion

5.1 Disc Simulations

5.1.1 Evolution of the SFR

Being interested in star formation, the first quantity we use to compare the two simulations is the disc's star formation rate. The star formation rates as well as a global star formation rate are calculated in HYDRA at each iteration. The total star formation rate (Ψ_{total}) of each disc was then plotted as a function of time (figure 5.1). It is worth noting that the global maxima in figure 5.1 are exaggerated as a product of the initial conditions used[1].

Figure 5.1 shows a peak in the total star formation rate for both models at the beginning of the simulation. Model-2 peaks to a higher total SFR than model-1 at the beginning of the simulation then decreases and falls below the the total SFR of model-1. This sudden decrease in the total SFR of model-2 is related to the feedback processes in the disc as mentioned before.

The $\nabla \cdot \vec{v} < 0$ condition in model-1 limits star formation to fewer regions (only collapsing regions). Therefore, model-1 is expected to have a lower total SFR as less

[1]There is a brief increase in the SFR due to cooling allowing the disc that is in hydrostatic equilibrium to collapse down before feedback can respond

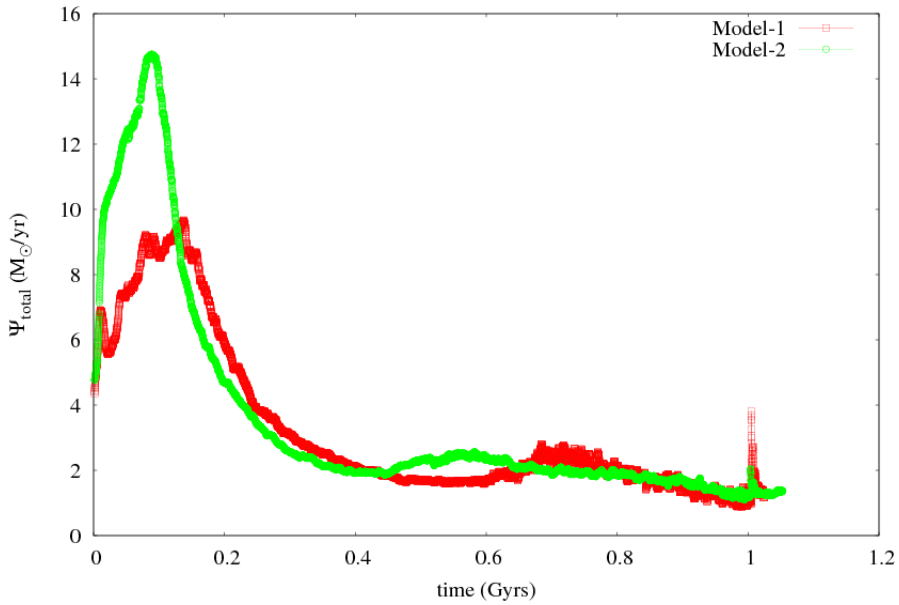

Figure 5.1: A comparison of the total SFR in both models. The two models seem to converge similar star formation rates as the simulation proceeds.

regions contribute to star formation. However, when comparing the total SFRs, both models seem to be similar. Model-2 exhibited more star formation at the beginning of the simulation and then converged to similar total SFR values as model-1 ($\Psi_{total} \sim 1.25 - 3 M_\odot/\mathrm{yr}$).

5.1.2 Filling Factors and Morphology

We first define some helpful terms. The filling factor is a count of the number of grid cells with a quantity value larger than a certain chosen minimum. The filling factor gives a direct representation of how a quantity changes as a function of a value. It is worth noting that the filling factor is a very poor measure of morphology as two systems with different overall appearances can still have the same filling factor. The filling ratio is the filling factor divided by the total number of cells in the grid.

Because of our interest in studying the effect of star formation algorithms on the morphology of galactic disc models, we compare the filling factor of different quantities (such as density, SFR) in both models. The two major quantities that we were interested in are the density, which directly describes the morphology of the disc, and the SFR which quantitatively describes the star forming regions. The filling factors for the two models was calculated at different times in the simulations for various minimum cut-off values.

Gas Density Filling Factor

The density filling factor summarizes some important information concerning the morphology of the disc reflecting whether there are some high density regions surrounded by less dense structures, or, for example, the whole galaxy is made of high density structures with few dense regions. We examined the density filling factor at different times in the simulations. The results are summarized in figure 5.2.

Early in the simulation, for $t \simeq 0.06$Gyr, both models had similar fill factors for all minimum cut-offs. This is expected because the two models started with the same initial conditions and star formation has had little chance to influence the overall evolution. Later in the simulation, at $t \simeq 0.95$Gyr, model-1 shows more dense regions than model-2 (model-1 had higher filling factors for higher density cut-offs). Therefore, removing the conditions on $\nabla \cdot \vec{v}$ places more feedback in high density regions, reducing the density and therefore limiting highest allowed densities. Such feedback can be studied by examining the temperature of the gas which directly influences its density. Model-2 shows more hot gas in the disc than model-1. Figure 5.3

demonstrates the difference in the temperature of the gas between the two models.

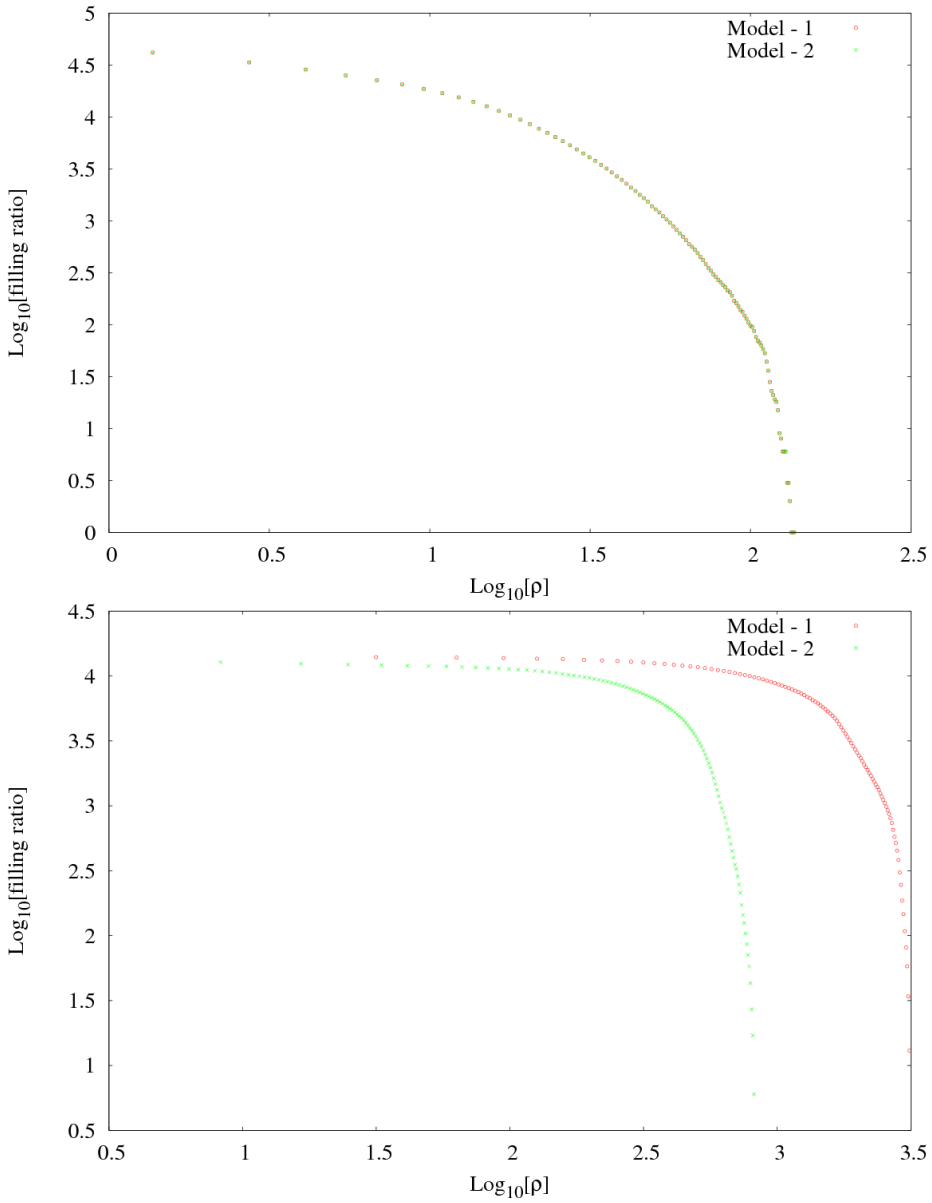

Figure 5.2: A plot of the density filling factor vs. the cut-off for which the filling factor is being evaluated. The density filling factor was evaluated at $t \simeq 0.06$Gyr (top), and $t \simeq 0.95$Gyr (bottom). Allowing star formation with no conditions on $\nabla \cdot \vec{v}$ limits the highest allowed densities in the galactic disc.

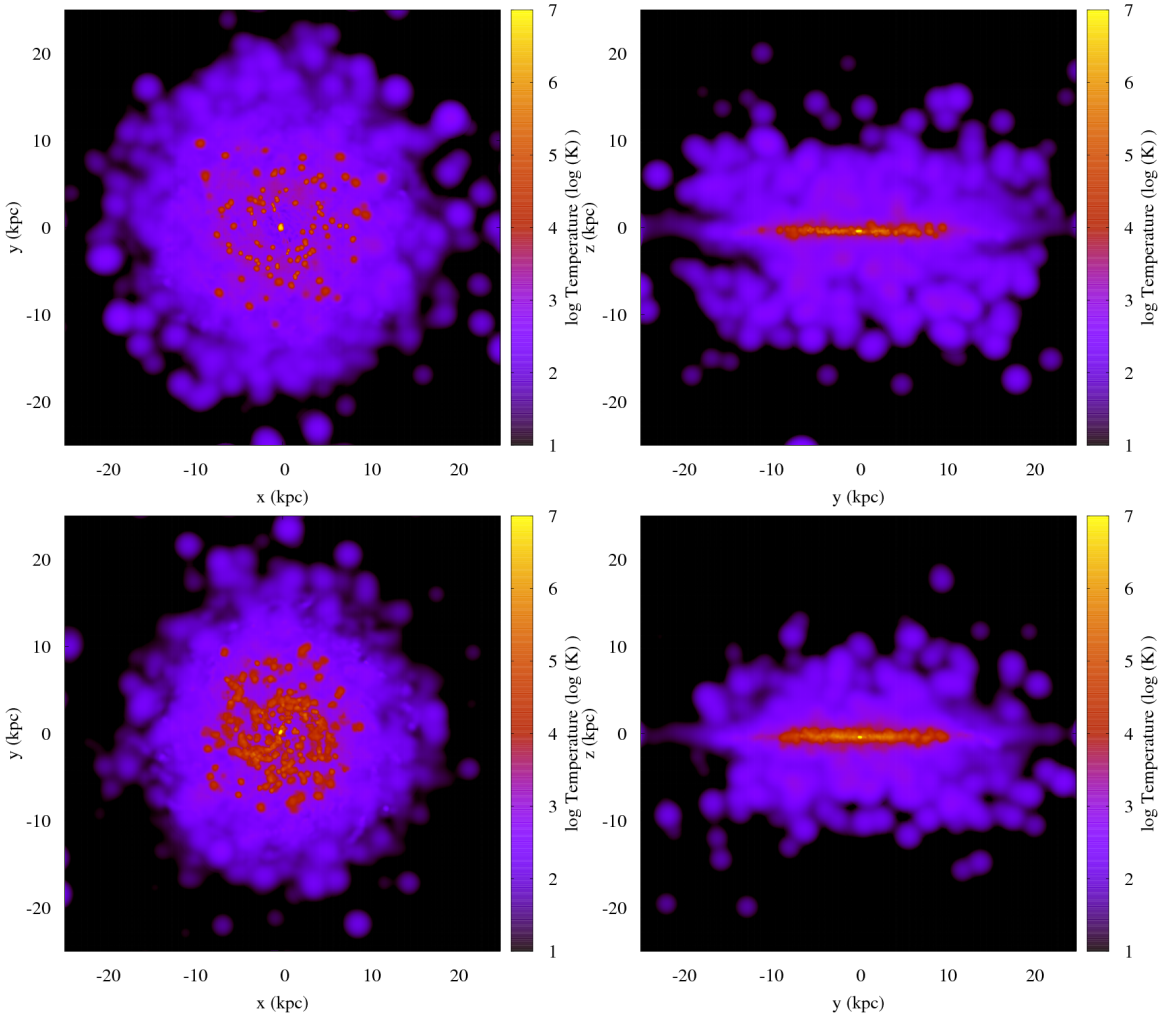

Figure 5.3: A plot of the temperature smoothed over a 1024×1024 grid. Model-2 (bottom) shows more hot gas in the disc than model-1 (top) which explains the presence of denser gas in model-1

SFR filling factor

Similar to the density filling factor, the SFR filling factor carries some important information about the star forming regions. It reflects whether the galaxy is having star-bursts in certain regions only or whether star formation is spread over the galaxy across a wider variety of environments. We examined the SFR filling factor at different times in the simulations, and the results are summarized in figure 5.4.

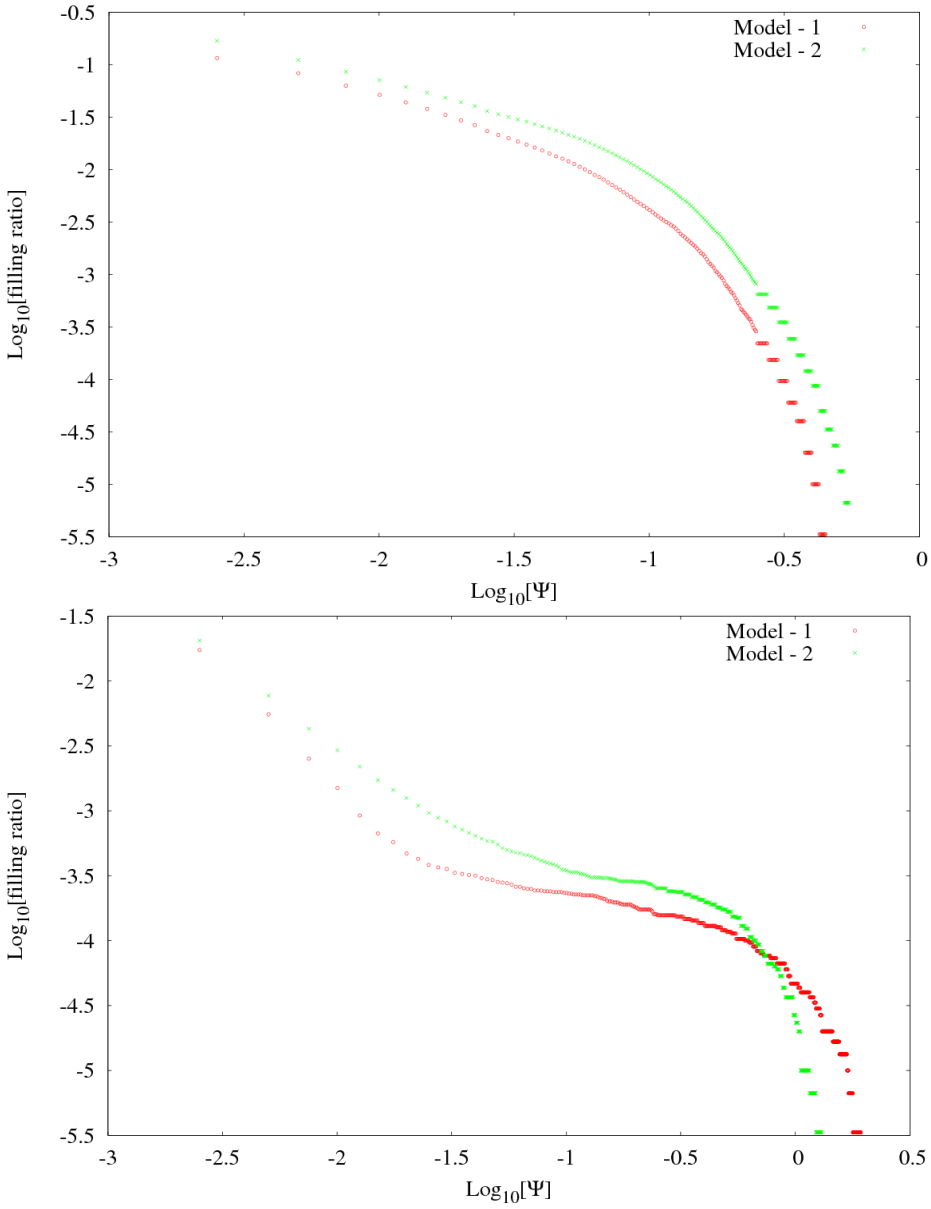

Figure 5.4: Evaluating the SFR filling factor at $t \simeq 0.06$Gyr (top), and $t \simeq 0.95$Gyr (bottom) shows that allowing star formation with no conditions on $\nabla \cdot \vec{v}$ limits the highest allowed SFR.

Early in the simulation, for $t \simeq 0.06$Gyr, model-2 had higher fill factors for all minimum cutoffs, which is expected because we had fewer conditions on star formation. This reflects that the algorithm found more star forming regions in model-2. Later in the simulation, at $t \simeq 0.95$Gyr, model-1 seemed to have more regions with

higher SFRs than model-2 (note that the two SFR curves cross-over). Therefore, allowing stars to form without any conditions on $\nabla \cdot \vec{v}$ limits the maximum allowed star formation rates which could be connected to various feedback processes. It is worth remembering that since the amount of gas is finite, starting with a high SFR will lead to a lower SFR as more gas is converted into stars. Therefore, model-1 will have a higher total SFR later during the simulation.

5.2 Cloud Simulations

The disc simulations showed slight differences between the two models. Because the discs have a large sheering rotation, the $\nabla \cdot \vec{v} < 0$ condition is exclusive to small local regions of high density. It is possible that the two different approaches applied to galaxy formation simulations could produce results far more different than those of the two disc simulations because the velocities (i.e. their 3D nature) are more complex. With more collapsing regions we expect to see more differences.

5.2.1 GSFR

The disc simulations started with an exaggerated peak in the total SFR. That peak is a product of the initial conditions. The clouds on the other hand, have a total SFR with various local maxima and minima and significantly higher dispersion in values. The total SFR of the clouds was plotted as a function of time as shown in figure 5.5.

The total SFRs of the two models are surprisingly similar. This leads to an interest in the number of stars formed in each cloud. The number of stars formed amounts

to an integral over the SFR (Ψ). The cumulative star count after every iteration was calculated and plotted as a function of time. Figure 5.6 demonstrates the cumulative star count at each iteration. Although both models had similar star formation rates, model-2 has significantly more stars forming.

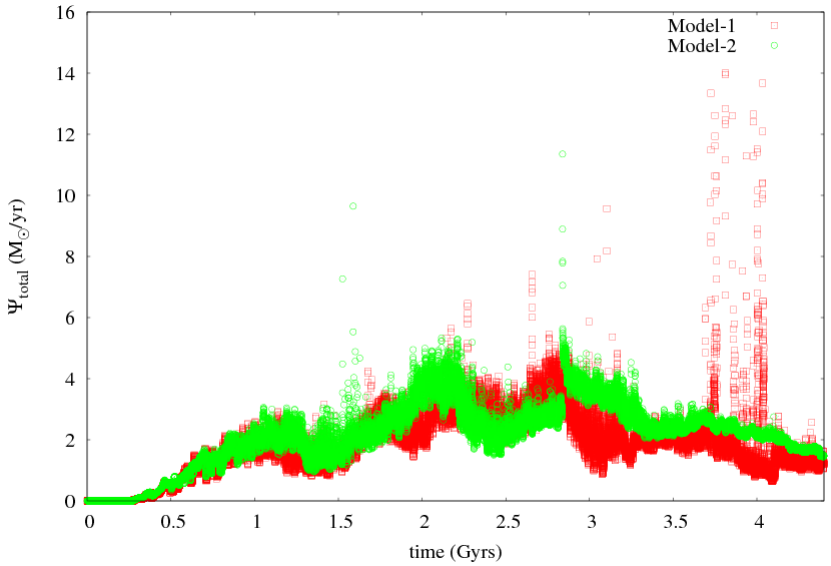

Figure 5.5: A comparison of the total star formation rates of the two models. Both models have similar star formation rates and high dispersion.

It is worth noting that removing the $\nabla \cdot \vec{v}$ condition caused some major differences in the stellar distribution between the two models (figure 4.3). Model-2 has a wider spread in the stellar distribution, as stars are not concentrated in the disc and the disc plane. This feature can be related to the fact that removing the velocity divergence criterion allowed stars to form in any dense and cool region. Therefore, as the clouds collapse, and fragmentation proceeds, more dense regions are formed allowing star formation in the halo as well, and hence the spread in the stellar population in model-2.

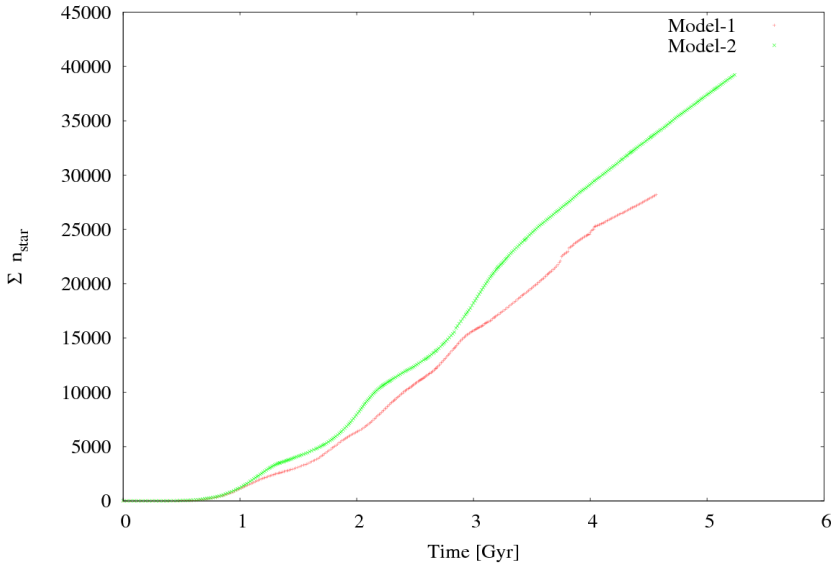

Figure 5.6: A comparison of the two models star count. Although both models share a similar total SFR, model-2 has a higher star count and therefore more star formation.

5.2.2 Phase Plots And Morphology

Temperature-Density (T-ρ) Phase Plots

T-ρ phase plots present a useful way of examining the state of the gas present and help us interpret the morphology of a cloud. The temperature and density are both values that are made available to us via the SPH method. Plotting temperature as a function of density, one is able to study distinct regions of the plot and draw some essential conclusions about the state of the gas in the simulation (Thacker and Couchman 2001). The following are 5 main regions in a T-ρ phase plot:

1. Hot low density gas: This is mainly gas in the halo that has been shock heated, or gas that has been heated and ejected into the halo by feedback.

2. Cold low density gas: This is the gas in the halo that has not been shock heated, or alternatively has been able to cool.

3. Cold high density gas: This is gas in collapsed clouds usually present in the disc.

4. Medium temp high density gas: This is gas in the disc that has yet to collapse into clouds, or cold gas that has been heated via feedback and is still in the process of cooling.

5. Hot high density gas: This is gas in the clouds that is being actively heated by the feedback processes.

Moreover, T-ρ phase plots facilitate tracking gas cycles in a galaxy where gas cycles between high density cold gas, to high density hot gas, then to lower density hot gas and eventually cooling down. In figure 5.7 we give the T-ρ phase plots for the two simulations at $t = 4.4$Gyr.

Model-2 lacks high density gas compared to model-1; this is evident in the truncation of the phase plot of model-2 at lower densities than that of model-1. Because no conditions on $\nabla \cdot \vec{v}$ are considered, the overall star formation rate in dense regions is higher. Therefore, dense gas regions form more stars causing the lack of dense gas. On the other hand, knowing that we are simulating a collapsing cloud, both models have shock heated gas (hot low density gas). Model-2 has more hot diffuse gas which is possibly caused by the ejection of gas into the halo due to feedback processes. Also, knowing that the stellar population in model-2 is not exclusive to the disc (see figure 4.3), the gas in the halo is more easily heated. Therefore, we detect the presence of more hot diffuse gas which is represented by a higher density of points in the T-ρ phase plots of model-2. Furthermore, model-1 lacks hot gas of medium density which

is expected with feedback processes limited to collapsing regions ($\nabla \cdot \vec{v} < 0$).

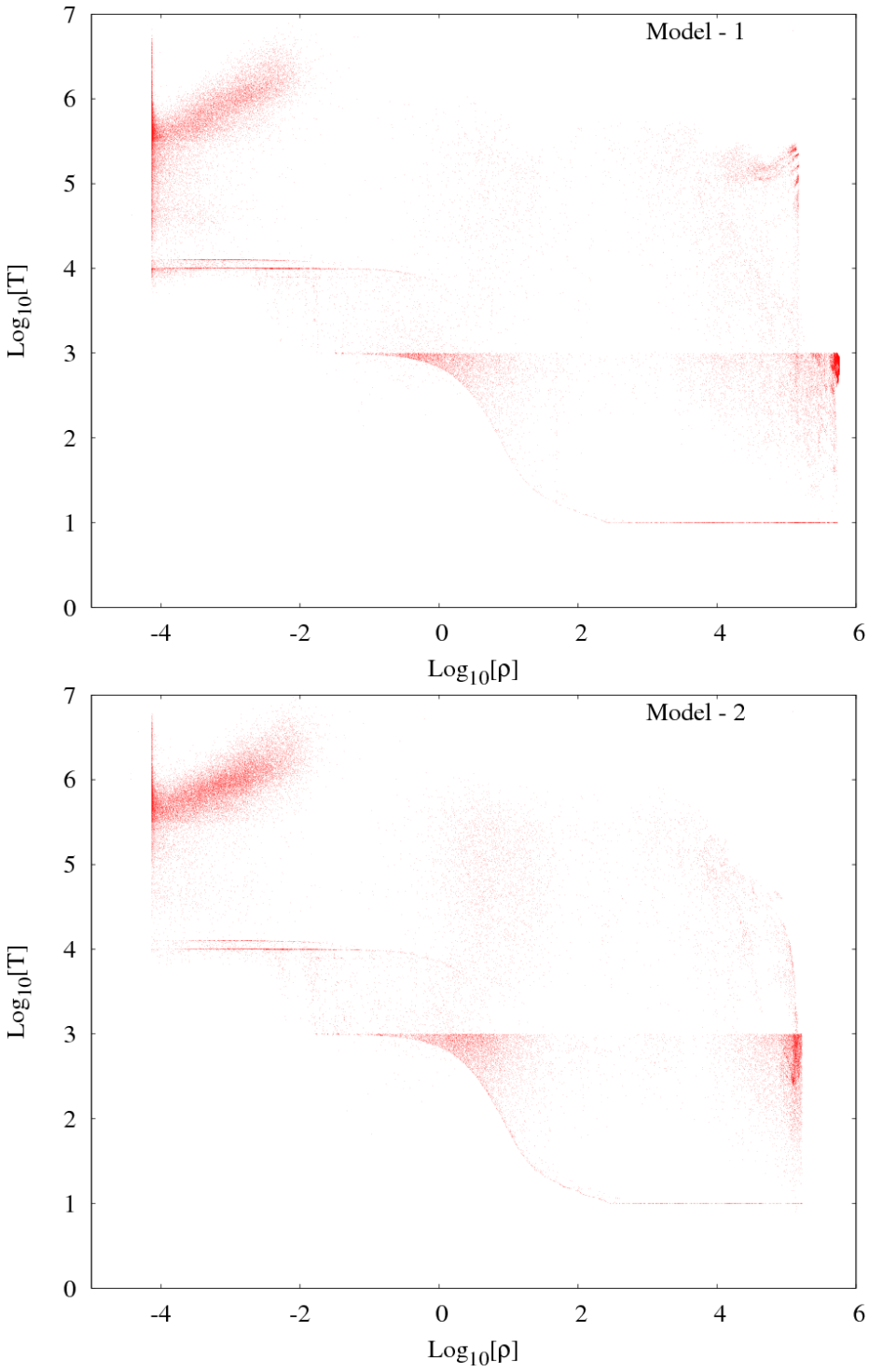

Figure 5.7: A temperature-density (T-ρ) phase plot of the two models. Model-1 (top) and model-2 (bottom) show significant differences.

Chapter 6

Conclusions and Future Work

6.1 Conclusions

The purpose of this thesis is to study the effects of different star formation algorithms on the morphology and star formation rates of galactic disc models. We ran two pairs of simulations using HYDRA_OMP, the parallel cosmological hydrodynamic code (Thacker and Couchman 2006), for a total of 369 hours of wall-clock time. Each pair of simulations differed in the star formation conditions used. Model-1, limited star formation to collapsing regions only ($\nabla \cdot \vec{v} < 0$), while model-2 had no conditions on $\nabla \cdot \vec{v}$. The simulations of the two discs were allowed to run for ~ 1.02Gyr, and those of the collapsing clouds (NFW profile) were allowed to run for ~ 4.4Gyr.

Disc Simulation

Removing the conditions on $\nabla \cdot \vec{v}$ caused more star formation which was reflected by the higher peak in the total SFR (figure 5.1). On the other hand, removing that condition reduced the highest allowed densities and SFRs which is depicted in the filling factor plots (see figures 5.2 and 5.4). Although they had different total SFRs at the beginning of the simulations, both models converged to similar total SFRs.

Cloud Simulation

The two cloud models show surprisingly similar total star formation rates (figure 5.5), but are morphologically distinct (see figures 4.2 and 4.3). Removing the condition on $\nabla \cdot \vec{v}$ caused more star formation (figure 5.6), as well as a reduction in the highest allowed gas densities (figure 5.7). Model-2 has gas of lower density when compared to model-1. Moreover, removing the $\nabla \cdot \vec{v}$ condition produced a lack of dense gas, and an abundance of hot diffuse gas, and hot medium density gas. Therefore, removing the $\nabla \cdot \vec{v}$ condition caused the formation of a larger halo populated with hot diffuse gas ejected from collapsing regions (see section 5.2.2). Moreover, removing the $\nabla \cdot \vec{v}$ condition lead to a spread in the stellar distribution to the halo (figure 4.3) which could be considered a major reason for the hot diffuse halo.

6.2 Future Work

The research, so far, has shown how changing the star formation algorithm can cause some major changes in the morphology of the system. Although some conclusions can be drawn from this research, significant work is still required to give quantitative conclusions in a cosmological context.

Additional low resolution analysis of distribution functions (mass and SFR) as well as volume and areal filling factors (ρ, SFR, and $\nabla \cdot \vec{v}$) is required. Studying the mass distribution function, and the SFR distribution function by mass of the discs and the collapsing clouds will have some important input on the differences in the morphology between the models. On the other hand, we have yet to examine

the cloud simulations' filling factors. It would be interesting to study the areal and volume filling factors of the cloud simulations which will highlight major differences between the two models (similar to the disc areal filling factor analysis). Moreover, it is important to consider calculating the filling factor of $\nabla \cdot \vec{v}$. By examining the divergence filling factor as well as the SFR and density filling factors, one can come to some conclusions on whether the conditions on $\nabla \cdot \vec{v}$ are the dominating conditions when forming stars in galaxy formation simulations. Completing the data analysis of the low resolution simulations would make it possible to start the next stage of this analysis and examining high resolution simulations of galaxy formation with cosmological initial conditions.

6.3 Acknowledgments

I would like to express my deepest gratitude to Professor Rob Thacker, my research supervisor, for his patient guidance, enthusiastic encouragement and useful critiques of this research work. I would also like to thank Mr. James Wurster for his encouragement, support, and helpful advice. Finally, as always, I am grateful and indebted to my family, whose value to me only grows with time.

Bibliography

[1] Benson A. J. Galaxy formation theory *Physics Reports*, 495pp 33-86, 2010.

[2] Blitz, L. Protostars and Planets III *ed E H Levy and J I Lunine (Tucson: University of Arizona Press)*, pp 125-61, 1999.

[3] Blitz, L., Williams, J. P. The Origin of Stars and Planetary Systems *ed C J Lada and N D Kylafis (Dordrecht: Kluwer)*, pp 328, 1999.

[4] Blumenthal G. R., Faber S. M., Primack J. R., Rees, M. J. Formation of galaxies and large-scale structure with cold dark matter *Nature*, 311pp 517-525, 1984.

[5] Carroll, B. W., Ostlie, D. A. An Introduction to Modern Astrophysics *Pearson Addison-Wesley Publishing Company, second edition*, 2007.

[6] Cole S., Aragon-Salamanca A., Frenk C. S., Navarro J. F., Zepf S. E. A Recipe for Galaxy Formation *Monthly Notices of the Royla Astronomical Society*, 271: 781, 1994.

[7] Couchman, H. M. P., Thomas, P. A., Pearce, F. R. *The Astrophysical Journal*, 452:797, 1995.

[8] Elmegreen, B. G. Protostars and Planets II *ed E H Levy and J I Lunine (Tucson: University of Arizona Press)*, pp 33-58, 1985.

[9] Elmegreen, B. G. Protostars and Planets II *ed E H Levy and J I Lunine (Tucson: University of Arizona Press)*, pp 97-124, 1993.

[10] Freeman K. C. On the Disks of Spiral and SO Galaxies *The Astrophysical Journal*, 160 881, 1970.

[11] Gingold, R. A., Monaghan, J. J. Smoothed particle hydrodynamics: theory and application to non-spherical stars *Monthly Notices of the Royal Astronomical Society*, 181:-389, 1977.

[12] Gingold, R. A., Monaghan, J. J. Kernel estimates as a basis for general particle methods in hydrodynamics *Journal of Computational Physics*, 46:-453, 1982.

[13] Hernquist, L., Katz, N. TreeSPH: a Unication of SPH with the Hierarchical Tree Method *The Astrophysical Journal Suppl. Ser.*, 70419, 1989.

[14] Hockney, R. W., Eastwood, J. W. Computer Simulation Using Particles *Institute of Physics Publishing*, 1988.

[15] Jeans, J. H. The Stability of a Spherical Nebula *Philosophical Transactions of the Royal Society of London*, Series A 199:-53, 1902.

[16] Katz, N. Dissipational galaxy formation. II - Effects of star formation *The Astrophysical Journal*, 391:502, 1992.

[17] Kennicutt, R. C. The Global Schmidt Law in Star-forming Galaxies *Astrophysical Journal*, 498:541, 1998.

[18] Komoroczi, A., Abe, S., Urai, J. L. Meshless numerical modeling of brittle-viscous deformation: first results on boudinage and hydrofracturing using a coupling of discrete element method (DEM) and smoothed particle hydrodynamics (SPH) *Computational Geosciences Journal*, 17:373-390, 2013.

[19] Lacey, C., Cole, S. Merger rates in hierarchical models of galaxy formation. *Monthly Notices of the Royal Astronomical Society*, vol. 262, no. 3 :627-649, 1993.

[20] Larson, R. B. The physics of star formation *Reports on Progress in Physics*, 66:pp 16-51, 2003.

[21] Li, Y., Mac Low, M. M., Klessen, R. S. Star Formation in Isolated Disk Galaxies. II. Schmidt Laws and Efficiency of Gravitational Collapse *Astrophysical Journal*, 639:879-896, 2006.

[22] Liu, G.R., Liu, M.B. Smoothed Particle Hydrodynamics - a Mesh-Free Particle Method. *World Scientific Publishing, Singapore*, 2003

[23] Lucy, L. B. A numerical approach to the testing of the fission hypothesis *Astronomical Journal*, 82:-324, 1977.

[24] Martin, C. L., Kennicutt, R. C. Star Formation Thresholds in Galactic Disks *Astrophysical Journal*, 555:301, 2001.

[25] McKee, C. F., Ostriker, J. P. A theory of the interstellar medium - Three components regulated by supernova explosions in an inhomogeneous substrate *Astrophysical Journal*, 218:148-169, 1977.

[26] Monaghan, J. J. Why Particle Methods Work *SIAM Journal on Scientific and Statistical Computing*, 3:, 1982.

[27] Monaghan, J. J. Smoothed particle hydrodynamics *Annual Reviews of Astronomy and Astrophysics*, 30:-574, 1992.

[28] Monaghan, J. J., Lattanzio, J. C. A refined method for astrophysical problems. *Astronomy and Astrophysics Journal*, 149:, 1985.

[29] Natanson, I. P. Theory of Functions of a Real Variable. *New York: Ungar*, 1960.

[30] Navarro, J.R., Frank, C.S.R. and White, S.D.M. The Structure of Cold Dark Matter Halos *Monthly Notices of the Royal Astronomical Society*, 1996.

[31] Navarro, J.R., Frank, C.S.R. and White, S.D.M. A Universal Density Profile from Hierarchical Clustering *The Astrophysical Journal*, 1997.

[32] Nguyen Luong, Q., Motte, F., Hennemann, M., Hill, T., Rygl, K. L. J., Schneider, N., Bontemps, S., Menshchikov, A., Andr, Ph., Peretto, N., Anderson, L. D., Arzoumanian, D., Deharveng, L., Didelon, P., Di Francesco, J., Griffin, M. J., Kirk, J. M., Knyves, V., Martin, P. G., Maury, A., Minier, V., Molinari, S., Pestalozzi, M., Pezzuto, S., Reid, M., Roussel, H., Sauvage, M., Schuller, F., Testi, L., Ward-Thompson, D., White, G. J. and Zavagno, A. The Herschel view of massive star formation in G035.3900.33: dense and cold filament of W48 undergoing a mini-starburst *Astronomy and Astrophysics Journal*, 535: 541, 2011.

[33] Peacock J. A. Cosmological Physics *Cambridge University Press, New York*, 2007.

[34] Robitaille, T. P., Whitney, B. A. The present-day star formation rate of the Milky-Way determined from Spitzer detected young stellar objects *The Astrophysical Journal, Letters*, 710:L11-L15, 2010.

[35] Rubin V. C., Ford W. K. Rotation of the Andromeda Nebula from a Spectroscopic Survey of Emission Regions *The Astrophysical Journal*, 159:379, 1970.

[36] Rygl, K. L. J., Wyrowski, F., Schuller, F., Menten, K. M. Initial phases of massive star formation in high infrared extinction clouds *Astronomy and Astrophysics Journal*, 515:A42,26, 2010.

[37] Schmidt, M. The Rate of Star Formation. *The Astrophysical Journal*, 129:243, 1959.

[38] Shapiro, P.R., Martel, H., Villumsen, J.V., Owen, J.M. Adaptive Smoothed Particle Hydrodynamics, with Application to Cosmology: Methodology *The Astrophysical Journal Supp. Ser.*, 103:269, 1996.

[39] Simon, R., Rathborne, J. M., Shah, R. Y., Jackson, J. M., Chambers, E. T. The Characterization and Galactic Distribution of Infrared Dark Clouds *The Astrophysical Journal*, 653:1325-1335, 2006.

[40] Solomon, P. M., Sanders, D. B. Protostars and Planets II *ed D C Black and M S Matthews (Tucson: University of Arizona Press)*, pp 59-80, 1985.

[41] Thacker, R. J., Couchman, H. M. P. Implementing Feedback in Simulations of Galaxy Formation: A Survey of Methods *The Astrophysical Journal*, 545:728, 2000.

[42] Thacker, R. J., Couchman, H. M. P. Star Formation, Supernovae Feedback and the Angular Momentum Problem in Numerical CDM Cosmogony: Half Way There? *The Astrophysical Journal, Letters*, 555:L17, 2001.

[43] Thacker, R. J., Couchman, H. M. P. A parallel adaptive P3M code with hierarchical particle reordering *Computer Physics Communications*, vol174, issue 7:pp 540-554, 2006.

[44] White S. D. M., Rees M. J. Core condensation in heavy halos - A two-stage theory for galaxy formation and clustering *Monthly Notices of the Royal Astronomical Society*, 183pp 341-358, 1987.

[45] Williams, J. P., Blitz, L., McKee, C. F. Protostars and Planets IV *Mannings et al (Tucson: University of Arizona Press)*, pp 97-120, 2000.

[46] Williamson, D. J., Thacker R. J. Effective viscosity from cloudcloud collisions in 3D global smoothed particle hydrodynamics simulations *Monthly Notices of the Royal Astronomical Society*, vol421, issue 3 2170-2186, 2012.

[47] Wurster, J., Thacker, R. J. A Comparative Study of AGN Feedback Algorithms *Monthly Notices of the Royal Astronomical Society*, Advance Access 22 :1993.